Applied Physics Letters

Submonolayer quantum dot quantum cascade long-wave infrared photodetector grown on Ge substrate

Cite as: Appl. Phys. Lett. **118**, 081102 (2021); https://doi.org/10.1063/5.0038844
Submitted: 26 November 2020 . Accepted: 10 February 2021 . Published Online: 23 February 2021

Zhijian Shen, Zhuo Deng, Xuyi Zhao, Jian Huang, Chunfang Cao, Xinbo Zou, Fengyu Liu, Qian Gong, and Baile Chen

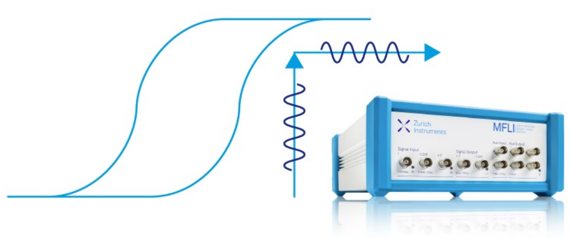

Submonolayer quantum dot quantum cascade long-wave infrared photodetector grown on Ge substrate

Cite as: Appl. Phys. Lett. **118**, 081102 (2021); doi: 10.1063/5.0038844
Submitted: 26 November 2020 · Accepted: 10 February 2021 ·
Published Online: 23 February 2021

View Online Export Citation CrossMark

Zhijian Shen,[1,2,3] Zhuo Deng,[1] Xuyi Zhao,[2] Jian Huang,[1] Chunfang Cao,[2] Xinbo Zou,[1] Fengyu Liu,[1] Qian Gong,[2,a)] and Baile Chen[1,a)]

AFFILIATIONS

[1]School of Information Science and Technology, ShanghaiTech University, Shanghai 201210, China
[2]Shanghai Institute of Microsystem and Information Technology, Chinese Academy of Sciences, Shanghai 200050, China
[3]University of Chinese Academy of Sciences, Beijing 100049, China

[a)]**Authors to whom correspondence should be addressed:** qgong@mail.sim.ac.cn and chenbl@shanghaitech.edu.cn

ABSTRACT

A germanium (Ge) or germanium-on-silicon (Ge-on-Si) substrate is an attractive yet not well-studied platform for developing long-wave infrared photonics devices such as lasers and photodetectors. In this paper, we report a long-wave infrared quantum cascade photodetector grown on the Ge substrate with a submonolayer InAs/GaAs quantum dot as the infrared absorber. At 77 K under zero bias, the detector shows a differential-resistance area (R_0A) product of 298.7 $\Omega\cdot$cm^2. The normal-incident peak responsivity is 0.56 mA/W observed at 8.3 μm, corresponding to a Johnson noise limited detectivity of 1.5×10^8 cm$\cdot$Hz$^{1/2}$/W. In addition, the effect of the periodic stage number of active regions on device's performance is discussed in detail. The device characteristics presented in this work demonstrate the potential for monolithic integration of this quantum cascade detector with the Ge or Ge-on-Si substrate for large-scale, cost-effective sensing and imaging applications.

Group IV photonic devices and systems have shown important applications in biochemical sensing, detection of toxics, industrial process control, and other areas.[1–3] The spectral range covered in these applications belongs to the long-wave infrared (LWIR) region, which is commonly referred to the fingerprint wavelength region (6–15 μm), since many molecules show strong vibrational absorption within this range.[3] Currently, silicon photonics based on silicon-on-insulator (SOI) has been widely employed for the photonic integrated circuits at telecommunication wavelengths (1.3 and 1.55 μm) due to the mature group IV material properties and fabrication processing.[4,5] Nevertheless, in fingerprint wavelength sensing and detection, a new material platform is imperative since silicon and silicon dioxide are lossy beyond 6 μm and cannot be used in the LWIR region.[3]

Recent studies have shown that the Ge-based material platform is an attractive alternative for integration with LWIR applications due to its wider infrared transmission window than Si (2–14 μm vs 1–6 μm).[3,6] Ge-on-Si-based planar photonic devices, such as low loss waveguides, multiplexers, and interferometers, have been demonstrated.[7] However, very few LWIR light sources and photodetectors on the Ge or Ge-on-Si substrate have been reported so far. Quantum cascade detectors (QCDs) based on quantum wells (QWs)[8] and quantum dots (QDs)[9,10] have long been the major choice for mid- and long-wave infrared (MWIR and LWIR) detection applications due to the high design freedom in the band structure and, hence, the operational wavelength. III–V materials such as GaAs and InP are the most commonly used substrates for quantum cascade photodetectors since they enjoy the merit of high crystalline compatibility. One way to build the inexpensive and compact photonic integrated devices is the heterogeneous integration by bonding III–V materials to the Ge-on-Si platform.[11] Nevertheless, the III–V substrates required for the bonding process are much more expensive than Si substrates and are only available at small wafer sizes that limit scalability. Alternatively, monolithic epitaxial growth is a straightforward wafer-level solution for low-cost and large-scale production.[12–15] In the MWIR range, monolithic growth of QCDs and other structures on Si has been successfully demonstrated.[12,16–19] For LWIR applications, it would be more desirable to grow the devices on Ge-on-Si substrates since Ge has a wider infrared transmission window.[3,6] Moreover, the Ge lattice constant is very close to that of GaAs (only 0.08% lattice mismatch), which could reduce the threading dislocation density as well.[20]

This work demonstrates the QCD grown on the Ge substrate for LWIR detection, which suggests that these LWIR devices could also be realized by epitaxial growth on Ge-on-Si substrates. The detector uses submonolayer (SML) InAs/GaAs QD structures to absorb infrared light and generate carriers, along with the GaAs/AlGaAs quantum cascade structures to extract electrons spontaneously. Similar to other QCD devices,[8,9,17,21] this detector enjoys the advantage of zero-bias operation. Given the 3D carrier confinement nature of SML QDs, this detector has both transverse magnetic (TM) and transverse electric (TE) optical responses.[9,10,17,22] In other words, the device can be operated in the normal incidence configuration, which can be potentially used for the focal plane array for target detection as well.

The schematics of the QCD device structure is illustrated in Fig. 1. The sample was grown on a Ge substrate by molecular beam epitaxy (MBE). A 1 μm GaAs buffer layer was grown before the photodetector heterostructure. 200 nm and 500 nm n-doped GaAs layers were used as the top and bottom contact layers, respectively. Two 50 nm $Al_{0.07}Ga_{0.93}As$ barriers were grown between the periodic quantum dot-quantum cascade stages and the n-doped GaAs top and bottom contacts to restrain the tunneling injection of electrons from the contacts. After that, the sample was composed of 20 periods of quantum dot-quantum cascade structures. For a single period, this quantum structure has two components: the optical transition region and the carrier extraction region. The optical transition region consists of five cycles of i-GaAs (2.10 ML)/n-InAs (0.37 ML, Si-doped, $n = 5 \times 10^{17}\,cm^{-3}$, 2 electrons/dot) SML QDs, sandwiched by 2 nm GaAs on each side. The carrier extraction region was composed of four GaAs/AlGaAs QWs, and the energy levels in those QWs were shifted subsequently such that their energy separation is equivalent to one GaAs LO phonon energy (~36 meV), enabling efficient carrier extraction. To minimize the accumulation of compressive strain, only one 3.8 nm $In_{0.15}Ga_{0.85}As$ QW was applied in the final QW, while the other three QWs were made from strain-free GaAs with an appropriate thickness. $Al_{0.2}Ga_{0.8}As$ barriers with a certain thickness were inserted between those QWs and SML QDs to separate them.

The number of stages of the active region is a key design parameter for QD-QCD, and an appropriate number would affect the device performance in terms of dark current, responsivity, and detectivity. For dark current (I_{dark}), this parameter is inversely proportional to the device differential resistance around 0 V (R_0)[8] and R_0 is proportional to the number of stages (N); thus, $I_{dark} \propto 1/N$. In other words, the increase in the stage number could help suppress the dark current. For responsivity, we have the following expressions:[8]

$$R = \frac{\lambda q}{hc}\eta\frac{p_e}{Np_c}, \tag{1}$$

$$\eta = 1 - e^{-N\alpha} \approx N\alpha, \quad \text{for } N\alpha \ll 1, \tag{2}$$

where R is the responsivity of QCDs, λ is the incident wavelength, η is the quantum efficiency, α is the absorption coefficient of SML QDs, p_e is the escape probability of an excited electron in the optical transition region, and p_c is the capture probability into next optical transition region's ground state for an electron traveling down the carrier extraction region. Under first-order approximation, when N is relatively small, $N\alpha \ll 1$, so $\eta \approx N\alpha$, and R remains constant regardless of the change in N. When N becomes larger, η approaches 1 and saturates. Thus, $R \propto 1/N$. In other words, with the increase in N, R remains constant at first and then decreases rapidly. For detectivity, since the noise of the QCD is mainly dominated by Johnson noise under zero bias, the detectivity can be written as[9,10,17,22]

$$D^* \approx D_j^* = R\sqrt{\frac{R_0 A}{k_B T}}, \tag{3}$$

where A is device's area, k_B is the Boltzmann constant, and T is the temperature. When N is relatively small, R remains constant and $R_0 \propto N$. Thus, $D^* \propto \sqrt{N}$. When N becomes larger, $R \propto 1/N$ and $R_0 \propto N$, which leads to $D^* \propto 1/\sqrt{N}$. That is to say, when N increases, D^* rises at the beginning and then falls. Therefore, an ideal number of stages must be picked by simultaneously taking the device's performance and epitaxial growth complexity into consideration, and this value is usually between 20 and 40.[23] We chose $N = 20$ as a preliminary starting point in this work.

The structure and growth conditions of this QCD grown on Ge were similar to the SML QD-QCD grown on the GaAs substrate reported by our group previously.[24] The growth temperature of the GaAs buffer, contacts, and the $Al_{0.07}Ga_{0.93}As$ barriers was 580 °C, whereas the absorption and cascade regions were grown at 500 °C. The energy levels and their corresponding wavefunctions in the conduction band calculated by the k·p method are shown in Fig. 2.[25–28] The red dashed arrows indicate that the transitions account for photocurrent, which include three basic steps in one period of the device: the optical transition ($E_1 \rightarrow E_2$), the electron transport from the optical transition region to the carrier extraction region through resonant tunneling ($E_2 \rightarrow E_3$), and the electron extraction ($E_3 \rightarrow E_4 \rightarrow E_5 \rightarrow E_6 \rightarrow E_1$). The solid gray arrow indicates the leakage path of dark current, which will be discussed later.

After the epitaxial growth, the crystal quality of the QCD sample was analyzed by high-resolution x-ray diffraction (XRD), as plotted in Fig. 3. Apart from the Ge (004) substrate reflection, the broad peak located at about 33.04° is contributed by the 20-period quantum dot-quantum cascade superlattice (labeled as SL) and the rest of the epilayers in the structure, i.e., GaAs buffer, contacts, and the $Al_{0.07}Ga_{0.93}As$ barrier layers, due to the very close lattice constant. Furthermore, clear satellite peaks of the SL are observed up to the fourth order. From the simulated

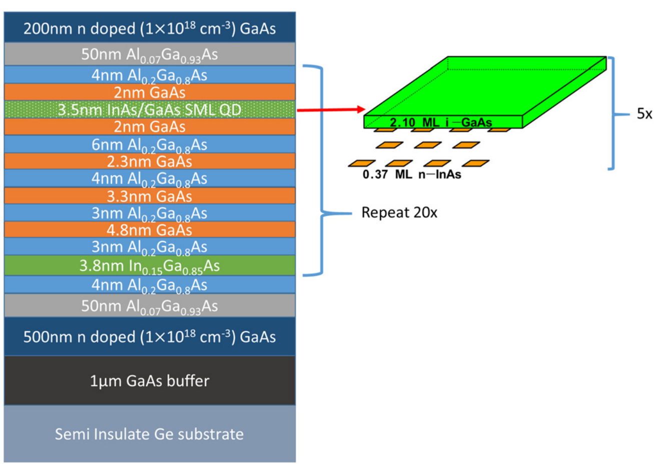

FIG. 1. The schematics of the SML QD-QCD device structure grown on the Ge substrate.

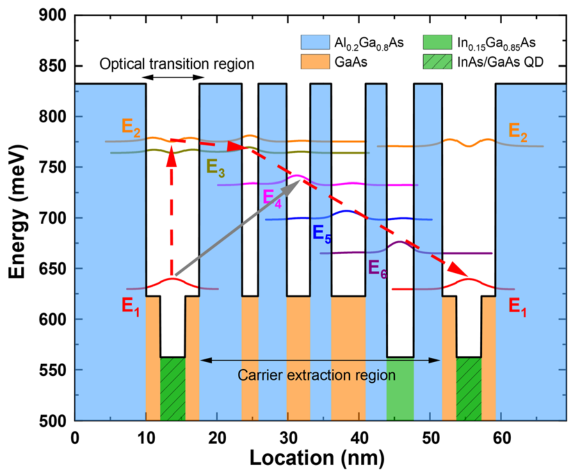

FIG. 2. Conduction band of one cycle of the SML QD-QCD's active region with energy levels and wavefunctions calculated by the k·p method. For illustration clarity, in the calculation, we set the thickness of $Al_{0.2}Ga_{0.8}As$ barriers on both sides with a relatively large thickness of 10 nm (vs 4 nm in Fig. 1). Starting from the left, the corresponding thickness of different layers is (in nm) **10**/2/3.5/2/**6**/2.3/**4**/3.3/**3**/4.8/**3**/*3.8*/**4**/2/3.5/2/**10**, with the $Al_{0.2}Ga_{0.8}As$ barrier in bold, the GaAs layer in regular, $In_{0.15}Ga_{0.85}As$ in italic, and InAs/GaAs QD underlined. The forbidden band corresponding to each layer was colored with the same coloring scheme as in Fig. 1. In order to simplify the calculation, the QD layers were treated as 3.5 nm $In_{0.15}Ga_{0.85}As$ layers. The red dashed arrows indicate the electronic extraction path of the device. The solid gray arrow represents the leakage path for dark current.

SL peak position, the thickness of the quantum dot-quantum cascade active region can be estimated as follows:[29]

$$d = \frac{\lambda}{2(\sin\omega_0 - \sin\omega_1)}, \tag{4}$$

where d is the thickness of one quantum dot-quantum cascade active region, λ is the wavelength of the x-ray source (0.15406 nm), and ω_0 and ω_1 are the central position of the zeroth order and first order SL peak, respectively. The calculated result shows that the thickness of one period of the active region is 42.1 nm, which is very close to the designed thickness shown in Fig. 1 (41.7 nm).

After material characterization, multiple mesa-isolated devices with different diameters ranging from 50 to 500 μm were processed using standard procedures, i.e., contact UV photolithography, wet chemical etching, electron-beam evaporation, and liftoff. The sidewalls of the devices were encapsulated with SU-8 negative photoresist to prevent the sidewall from degradation.

Figure 4 depicts the dark current density-bias (J–V) characteristics of the SML QD-QCD sample with a diameter of 130 μm measured at various temperatures. During the measurement, the sample was loaded in a variable-temperature cryostat and isolated with a cold shield and aluminum foil from background radiation, and the data were collected and analyzed using a semiconductor device analyzer. As seen from Fig. 4, the device shows a dark current density of 2.5×10^{-4} A/cm^2 at 77 K under -0.1 V bias and increases rapidly with external reverse bias, indicating the resonant tunneling transport of carriers in the device. In order to find out the main source of dark current, the differential resistance-area product (R_0A) at different temperatures is derived from the slope of the J–V curves around zero bias, as shown in Fig. 5. The R_0A value is 298.7 $\Omega\cdot$cm^2 at 77 K and decreases to 9.7×10^{-3} $\Omega\cdot$cm^2 at room temperature. The data are fitted by the Arrhenius equation as follows:[30]

$$R_0A = Ce^{-\frac{E_a}{k_B T}}, \tag{5}$$

where C is the Arrhenius constant and E_a is the activation energy. In the low-temperature region (77 K–190 K), the approximated activation energy is $E_a \sim 108.8$ meV, which is about three times of the GaAs LO phonon energy (3×36 meV). This suggests that the major leakage path for dark current in this QCD device might be the diagonal transition from the quantum dot region to the second quantum cascade level, $E_1 \rightarrow E_4$, as illustrated in Fig. 2.[9,17,24]

After the electrical characterization, a 130 μm device used in the dark current measurement was wire bonded and loaded into a cryostat and refrigerated to 77 K using liquid nitrogen. The sample was

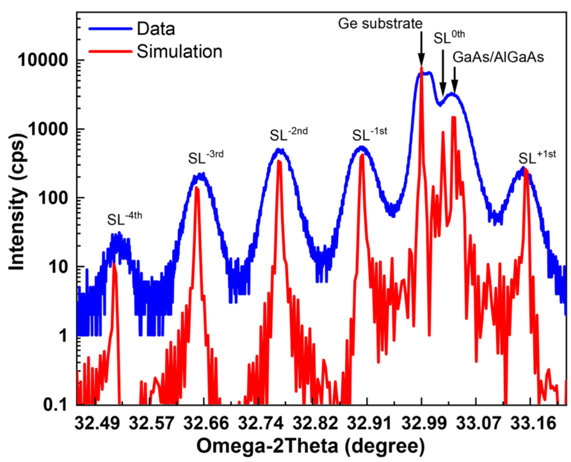

FIG. 3. XRD ω-2θ scan of the SML QD-QCD sample grown on Ge. The blue curve represents the measurement data, while the red curve is the simulation result.

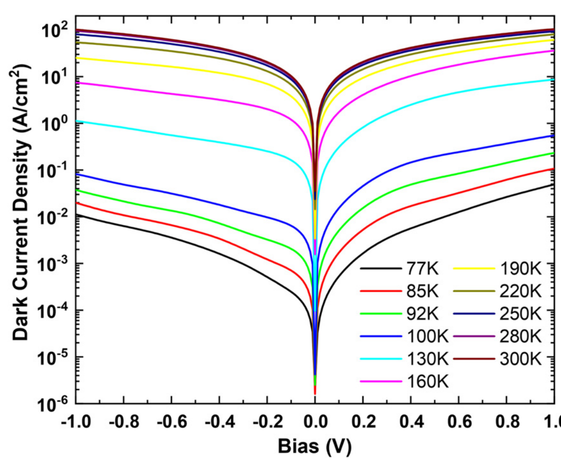

FIG. 4. Dark current density-bias voltage curves of the SML QD-QCD with a diameter of 130 μm measured from 77 to 300 K.

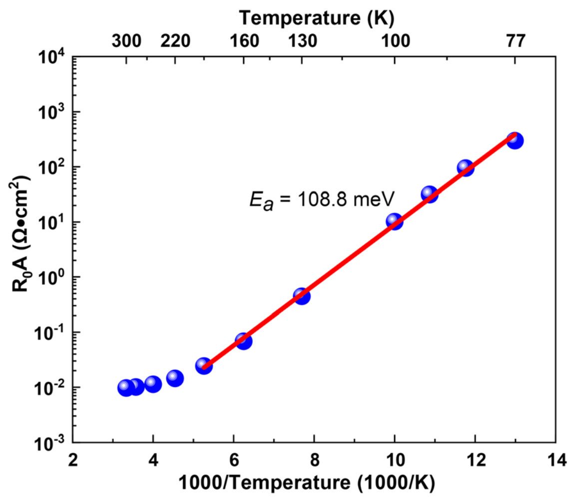

FIG. 5. R_0A product-inverse temperature dependences of the 130 μm diameter device. The blue dots are R_0A values from 77 K to 300 K, and the red line is the fitted curve with the Arrhenius equation. The fit was only performed for data from 77 K to 190 K due to the deviation from linearity at high temperature.

configured in normal incidence without any antireflection (AR) coating. The optical response of the sample was collected and analyzed using a Fourier transform infrared spectrometer (FTIR) and calibrated by a 700 °C blackbody source. Figure 6 depicts the responsivity of the device measured from 77 K to 92 K without any applied bias, covering a spectral range from 6.5 μm to 10.0 μm. The maximum responsivity of the device is 0.56 mA/W at 77 K, and its peak wavelength is around 8.3 μm (~149 meV). This energy is associated with the inter-subband transition from the SML QD ground state to the excited state, which is consistent with the designed energy separation between E_1 and E_2 (~145 meV), as shown in Fig. 2. It is worth mentioning that the peak responsivity in this device is an order of magnitude lower than that of the QCD device reported by us with the same active region but grown on the native GaAs substrate.[24] This might be due to the defects associated with the antiphase boundaries at the Ge/GaAs interface, even though the lattice mismatch with the Ge substrate is less than that compared with Si,[31] which could shorten the carrier lifetime and, hence, the responsivity. Further optimization in reducing the number of defects propagating from the Ge/GaAs interface into the active region in this SML QD-QCD device will be the theme of our future work.

Finally, the Johnson noise-limited detectivity D_j^* of the device is calculated using Eq. (3). Figure 7 shows the calculated D_j^* of the SML QD-QCD device from 77 K to 92 K. At 77 K, a peak value of 1.5×10^8 cm·Hz$^{1/2}$/W is observed. The peak detectivity of this QCD grown on Ge is close to that of the LWIR quantum dash QCD device grown on the native InP substrate reported by Wang *et al.*[32] ($D_j^* = 2 \times 10^8$ cm·Hz$^{1/2}$/W at 77 K and 0 V, peak at 10 μm). However, the relatively low responsivity of our device when compared with that in the work of Wang *et al.* and other QD-QCDs working at similar wavelengths[22,32] suggests that further improvements over this unoptimized design should be directed toward the absorber region, such as increasing the active doping density of the QDs[8] and suppressing the density of defects in the absorber, which might originate from the Ge/GaAs interface.

To summarize, a normal-incident, zero-bias operable LWIR QCD grown on the Ge substrate with submonolayer InAs/GaAs QDs as an absorber has been demonstrated and characterized. At 77 K, the device has a peak responsivity of 0.56 mA/W at 8.3 μm under zero bias and an R_0A value of 298.7 Ω·cm^2. The corresponding Johnson noise-limited detectivity is 1.5×10^8 cm·Hz$^{1/2}$/W. The performance of the device can be further strengthened by redesigning the device structure, such as increasing the doping density in the absorber and improving the epitaxial quality of the Ge/GaAs interface. The characterization results presented in this work pave the way for monolithic integration of InAs-based SML QD-QCDs with the Ge or Ge-on-Si substrate toward large-scale, low-cost LWIR sensing and imaging applications.

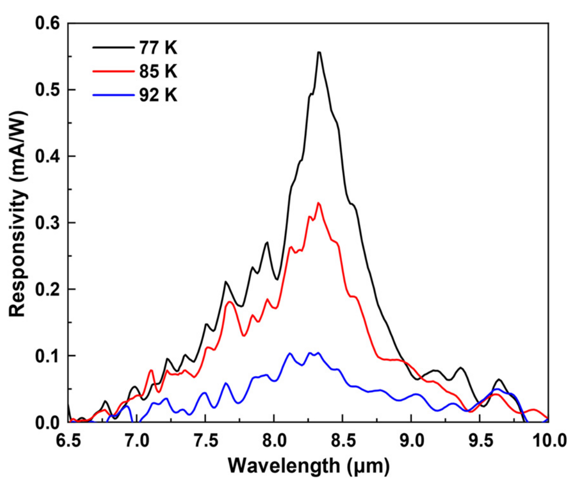

FIG. 6. Photoresponse under the normal incidence of the SML QD-QCD device measured at 77 K, 85 K, and 92 K under zero bias.

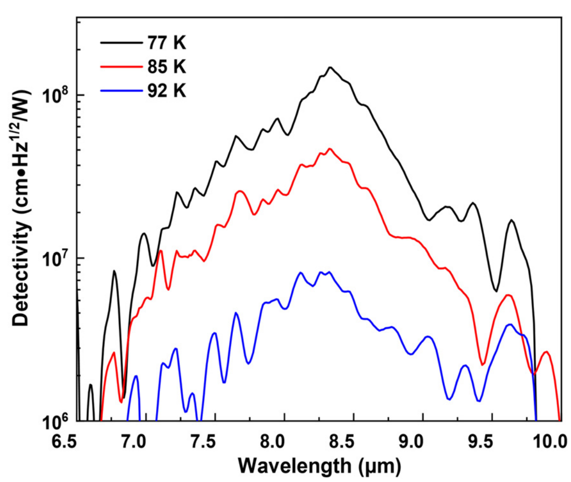

FIG. 7. The calculated D_j^* of the SML QD-QCD device at 77 K, 85 K, and 92 K under zero bias.

AUTHORS' CONTRIBUTIONS

Z.S., Z.D., and X.Z. contributed equally to this work.

This work was supported in part by the National Key Research and Development Program of China under Grant No. 2019YFB2203400 and the National Natural Science Foundation of China under Grant No. 61975121.

DATA AVAILABILITY

The data that support the findings of this study are available from the corresponding authors upon reasonable request.

REFERENCES

[1]A. Fernández Gavela, D. Grajales García, J. C. Ramirez, and L. M. Lechuga, Sensors **16**(3), 285 (2016).
[2]E. Descrovi, F. Frascella, B. Sciacca, F. Geobaldo, L. Dominici, and F. Michelotti, Appl. Phys. Lett. **91**(24), 241109 (2007).
[3]R. Soref, Nat. Photonics **4**(8), 495–497 (2010).
[4]D. Liang and J. E. Bowers, Nat. Photonics **4**(8), 511–517 (2010).
[5]G. T. Reed, G. Mashanovich, F. Y. Gardes, and D. J. Thomson, Nat. Photonics **4**(8), 518–526 (2010).
[6]G. Z. Mashanovich, C. J. Mitchell, J. S. Penades, A. Z. Khokhar, C. G. Littlejohns, W. Cao, Z. Qu, S. Stanković, F. Y. Gardes, and T. B. Masaud, J. Lightwave Technol. **35**(4), 624–630 (2017).
[7]Y.-C. Chang, V. Paeder, L. Hvozdara, J.-M. Hartmann, and H. P. Herzig, Opt. Lett. **37**(14), 2883–2885 (2012).
[8]F. R. Giorgetta, E. Baumann, M. Graf, Q. Yang, C. Manz, K. Kohler, H. E. Beere, D. A. Ritchie, E. Linfield, and A. G. Davies, IEEE J. Quantum Electron. **45**(8), 1039–1052 (2009).
[9]J. Huang, D. Guo, W. Chen, Z. Deng, Y. Bai, T. Wu, Y. Chen, H. Liu, J. Wu, and B. Chen, Appl. Phys. Lett. **111**(25), 251104 (2017).
[10]X.-J. Wang, S.-Q. Zhai, N. Zhuo, J.-Q. Liu, F.-Q. Liu, S.-M. Liu, and Z.-G. Wang, Appl. Phys. Lett. **104**(17), 171108 (2014).
[11]A. Spott, J. Peters, M. L. Davenport, E. J. Stanton, C. D. Merritt, W. W. Bewley, I. Vurgaftman, C. S. Kim, J. R. Meyer, J. Kirch, L. J. Mawst, D. Botez, and J. E. Bowers, Optica **3**(5), 545 (2016).
[12]J. Wu, Q. Jiang, S. Chen, M. Tang, Y. I. Mazur, Y. Maidaniuk, M. Benamara, M. P. Semtsiv, W. T. Masselink, and K. A. Sablon, ACS Photonics **3**(5), 749–753 (2016).
[13]Y. Wan, S. Zhang, J. C. Norman, M. J. Kennedy, W. He, S. Liu, C. Xiang, C. Shang, J.-J. He, A. C. Gossard, and J. E. Bowers, Optica **6**(11), 1394 (2019).
[14]J. C. Norman, D. Jung, Y. Wan, and J. E. Bowers, APL Photonics **3**(3), 030901 (2018).
[15]B. Chen, Y. Wan, Z. Xie, J. Huang, N. Zhang, C. Shang, J. Norman, Q. Li, Y. Tong, and K. M. Lau, ACS Photonics **7**(2), 528–533 (2020).
[16]B. Dror, Y. Zheng, M. Agrawal, K. Radhakrishnan, M. Orenstein, and G. Bahir, IEEE Electron Device Lett. **40**(2), 263–266 (2019).
[17]J. Huang, D. Guo, Z. Deng, W. Chen, H. Liu, J. Wu, and B. Chen, J. Lightwave Technol. **36**(18), 4033–4038 (2018).
[18]Q. Durlin, J. P. Perez, L. Cerutti, J. B. Rodriguez, T. Cerba, T. Baron, E. Tournié, and P. Christol, Infrared Phys. Technol. **96**, 39–43 (2019).
[19]W. Chen, Z. Deng, D. Guo, Y. Chen, Y. I. Mazur, Y. Maidaniuk, M. Benamara, G. J. Salamo, H. Liu, J. Wu, and B. Chen, J. Lightwave Technol. **36**(13), 2572–2581 (2018).
[20]H. Liu, T. Wang, Q. Jiang, R. Hogg, F. Tutu, F. Pozzi, and A. Seeds, Nat. Photonics **5**(7), 416 (2011).
[21]D. Hofstetter, M. Beck, and J. Faist, Appl. Phys. Lett. **81**(15), 2683–2685 (2002).
[22]A. V. Barve and S. Krishna, Appl. Phys. Lett. **100**(2), 021105 (2012).
[23]B. Schwarz, P. Reininger, A. Harrer, D. MacFarland, H. Detz, A. M. Andrews, W. Schrenk, and G. Strasser, Appl. Phys. Lett. **111**(6), 061107 (2017).
[24]Z. Shen, Z. Deng, X. Zhao, J. Huang, L. Yao, X. Zou, C.-F. Cao, Q. Gong, and B. Chen, "Long-wave infrared sub-monolayer quantum dot quantum cascade photodetector," J. Lightwave Technol. (published online).
[25]B. Chen, IEEE Trans. Electron Devices **64**(4), 1606–1611 (2017).
[26]B. Chen, W. Y. Jiang, and A. L. Holmes, Opt. Quantum Electron. **44**(3-5), 103–109 (2012).
[27]B. Chen, Opt. Express **25**(21), 25183–25192 (2017).
[28]B. Chen and A. L. Holmes, Opt. Quantum Electron. **45**(2), 127–134 (2013).
[29]A. Krost, G. Bauer, and J. Woitok, in *Optical Characterization of Epitaxial Semiconductor Layers*, edited by G. Bauer and W. Richter (Springer Berlin Heidelberg, Berlin, Heidelberg, 1996), pp. 287–391.
[30]X. Li, J. E. Carey, J. W. Sickler, M. U. Pralle, C. Palsule, and C. J. Vineis, Opt. Express **20**(5), 5518–5523 (2012).
[31]I. Nemeth, B. Kunert, W. Stolz, and K. Volz, *Microscopy of Semiconducting Materials 2007* (Springer, 2008), pp. 107–110.
[32]F.-J. Wang, F. Ren, S.-M. Liu, N. Zhuo, S.-Q. Zhai, J.-Q. Liu, F.-Q. Liu, and Z.-G. Wang, Nanoscale Res. Lett. **11**(1), 392 (2016).